RSC Applied Interfaces

ROYAL SOCIETY OF CHEMISTRY

PAPER

View Article Online
View Journal | View Issue

Cite this: *RSC Appl. Interfaces*, 2025, **2**, 1311

Hollow SnO_2 nanosphere-coated separators for dendrite-free lithium metal batteries†

Yi Chen, Xingyan Zeng, Yufei Yang, Xuyang Wang, Hui Nie, * Xingping Zhou and Xiaolin Xie

Serious dendrite formation remains a significant challenge for the practical application of high-energy lithium metal batteries (LMBs). Fabricating separators with a high lithium ion transference number (t_{Li^+}) and uniform pore structure is an effective strategy to homogenize Li^+ flux and suppress dendrite growth. Here, hollow SnO_2 nanospheres with high structural stability were synthesized through a solvothermal method for surface coating of a poly(ethylene-*co*-acrylic acid) (EAA) separator (EAA@SnO_2). The EAA matrix enhances the t_{Li^+} through the interaction of carboxyl groups with ions in the electrolyte, while hollow SnO_2 nanospheres convert to Li_xSn during cycling, regulating Li^+ flux and promoting uniform solid electrolyte interphase formation. The as-prepared separator-based Li symmetric cells demonstrate stable cycling for over 1000 h with a low overpotential of 17 mV. Additionally, the $LiFePO_4$||Li cells with the EAA@SnO_2 separator deliver an initial capacity of 116.6 mA h g^{-1} and a capacity retention of over 80.96% after 200 cycles at 5C. The utilization of metallic hollow SnO_2 nanospheres for separator coating proves to be a promising strategy for high-performance LMBs.

Received 11th April 2025,
Accepted 28th May 2025

DOI: 10.1039/d5lf00101c

rsc.li/RSCApplInter

Introduction

Lithium metal batteries (LMBs) are regarded as the "holy grail" of next generation batteries due to its exceptional theoretical capacity of 3860 mA h g^{-1} and the lowest redox potential of −3.04 V.[1,2] Nevertheless, the Li metal reacts with electrolytes during cycling due to its high reactivity, leading to an unstable solid electrolyte interface (SEI) and severe dendrite growth.[3,4] These challenge results in the reduced Coulombic efficiency and poor cycling stability, ultimately impeding the practical application of LMBs.[5,6] Until now, strategies such as modification of anodes,[7–9] electrolyte additives,[10,11] solid-state electrolytes[12–14] and artificial SEIs[15,16] have been developed to address the above issues. Among them, the design of a functional separator presents an effective approach to mitigate the above issues.

The separator in batteries isolates the cathode and anode while allowing the transport of Li^+ through its porous structure. Nonpolar polyolefin separators exhibit a non-uniform porous structure, which consequently leads to an inhomogeneous Li^+ flux and accelerates the dendrite growth.[17,18] Moreover, according to Sand's time, the cells with those separators with a high lithium ion transference number (t_{Li^+}) exhibit a reduced propensity for dendrite formation while the t_{Li^+} of polyolefin separators is only 0.2–0.4.[19,20] Various strategies have been developed to mitigate the issue of dendrite growth. It has been demonstrated that increasing the polarity of separators enhances their interaction with ions in the electrolytes, thereby increasing the t_{Li^+}.[21,22] One effective strategy is the modification of polyolefin separators with polar polymers,[23,24] inorganic compounds,[25,26] metal–organic frameworks,[27–29] or covalent organic frameworks.[30,31] Another strategy for suppressing dendrite growth is fabrication of separators using polar polymers, including polyimide (PI),[32,33] polyether ether ketone (PEEK)[34,35] and poly(vinylidene fluoride) (PVDF).[36] In our previous work, the poly(ethylene-*co*-acrylic acid) (EAA) separator has been fabricated by a facile template etching method. The carboxyl groups in the EAA layer of this separator significantly enhance the t_{Li^+} and inhibit the dendrite growth, which has been proved by solid nuclear magnetic resonance spectroscopy and molecular dynamics simulations.[37]

Except increasing t_{Li^+}, regulating the Li^+ flux is another effective way to promote homogenous Li^+ deposition. Metallic materials such as Mg,[38] Au,[39] Cu[40] and Ge[41] have been incorporated into separators to regulate the Li^+ flux due to their lithiophilic properties. Among them, Sn is particularly promising due to its similar nucleation overpotential to lithium, which facilitates homogeneous lithium plating/stripping.[42]

Key Laboratory of Material Chemistry for Energy Conversion and Storage, Ministry of Education, School of Chemistry and Chemical Engineering, Huazhong University of Science and Technology, Wuhan 430074, China. E-mail: huinie@hust.edu.cn

† Electronic supplementary information (ESI) available: XPS, pore distribution and EDX mapping of SnO_2; LSV, CV and EIS of EAA@SnO_2 separators; photographs of symmetric cells. See DOI: https://doi.org/10.1039/d5lf00101c

SnO_2 has been utilized in separators of Li–S batteries for its adsorption and catalytic abilities.[43–45] In addition, SnO_2 converts to lithiophilic Li_xSn alloys with a two-step reaction, which is beneficial for uniform Li deposition.[46,47] However, serious volume expansion (>300%) happens during this process, which hinders their further application.[48]

In this study, hollow SnO_2 nanospheres were synthesized and coated on the surface of EAA porous separators, forming EAA@SnO_2 composite separators. The incorporation of hollow SnO_2 nanospheres to separators facilitates the alloying with lithium, thereby constructing a uniform electric field and forming a smooth SEI. This unique hollow structure provides sufficient space to accommodate the volume expansion of Sn while ensuring a homogeneous Li^+ flux. Furthermore, the carboxyl groups on the EAA layer boost the t_{Li^+} of separator to 0.74. The synergistic effect of EAA and SnO_2 effectively suppresses dendrite growth, resulting in a dendrite-free anode. Notably, the EAA@SnO_2 assembled Li symmetric cell could cycle for over 1000 h at a current density of 0.5 mA cm^{-2} with an overpotential of 17 mV. Impressively, the EAA@SnO_2-based $LiFePO_4$ (LFP)||Li cells maintain a capacity retention of over 80.96% at 5C after 200 cycles. Our research indicates that the EAA@SnO_2 separator holds significant promise for application in fast-charging LMBs.

Experimental

Materials

Ethylene acrylic acid 6100 (EAA 6100) was purchased from SK Chemicals (the content of acrylic acid is 10 wt%). Polyethylene glycol 2000 (PEG 2000), hydrochloric acid (HCl, 36.5–38 wt%), tetrahydrofuran (THF) and ethanol (EtOH) were purchased from Sinopharm Chemical Reagent Co. (Shanghai, China). Tin tetrachloride ($SnCl_4{\cdot}5H_2O$) and polyacrylic acid (PAA) were purchased from Aladdin Biochemical Technology Co., Ltd. (Shanghai, China). The liquid electrolyte of 1 mol L^{-1} $LiPF_6$ in a mixed solvent [V(EC):V(DEC) = 1:1] was purchased from Duoduo Chemical Reagent Network. Polyethylene (PE) was obtained from Jiangsheng Material Co. (Hubei, China).

Preparation of hollow SnO_2 nanospheres

Hollow SnO_2 nanospheres were synthesized by a hydrothermal method. 0.38 g $SnCl_4{\cdot}5H_2O$ was dissolved in a mixture of 4 mL deionized water and 40 mL EtOH followed by 1 mL HCl. The solution was stirred for 30 min to obtain a homogeneous solution. After that, the solution was transferred into a Teflon-lined stainless-steel autoclave and heated at 200 °C for 24 h. Then, the solution was cooled to room temperature naturally. The obtained product was washed with deionized water and ethanol several times to remove the impurities and dried at 60 °C overnight.

Preparation of EAA@SnO_2 separators

The preparation of the EAA separator was based on our previously developed fabrication procedures.[37] 0.7 g EAA and 0.5 g PEG 2000 were dissolved in 10 mL THF with magnetic stirring at 65 °C for 1 h. The resulting solution was then cast onto a glass substrate using a 750 μm doctor blade at 60 °C. After standing for 1 min, the substrate was immersed in water to remove the THF and PEG 2000. The EAA separator was then transferred to ethanol and dried at room temperature.

25 mg SnO_2 was dispersed in 10 mL EtOH with 2.5 mg PAA as a binder and ultrasonicated for 30 min. After that, the SnO_2 dispersion was sprayed onto the EAA separator with a pressure of 0.1 MPa and a distance of 10 cm, and dried naturally to obtain the EAA@SnO_2 separator.

Characterization

Crystallinity of the as-prepared SnO_2 was characterized by X-ray powder diffraction (XRD, XRD-7000) analysis with Cu-Kα (λ = 1.54178 Å) radiation with 2θ ranging from 20–80° at a scanning rate of 5° min^{-1}. The morphology of SnO_2 was characterized by transmission electron microscopy (TEM, HT7800), high-resolution transmission electron microscopy (HRTEM, Talos F200X) and scanning electron microscopy (SEM, Hitachi S-4700). The microstructure of the EAA@SnO_2 separators was characterized by SEM. The contact angle between the separators and liquid electrolyte was evaluated using a contact angle tester (OCA20).

Electrochemical measurements

Ionic conductivity was determined by electrochemical impedance spectroscopy (EIS) using an Autolab PGSTAT302N, and calculated *via* the following equation:

$$\sigma = \frac{d}{R_d \times S} \quad (1)$$

where d, R_d and S are the thickness of the separator, bulk resistance and the area of the electrode, respectively.

The electrochemical stability was measured from liner sweep voltammetry (LSV) from 0 to 7.0 V at a scan rate of 1 mV s^{-1}.

The lithium ion transference number (t_{Li^+}) was evaluated by combining chronoamperometry and EIS analysis using Li symmetric cells. t_{Li^+} was calculated according to the following equation:

$$t_{Li^+} = \frac{I_s(\Delta V - I_0R_0)}{I_0(\Delta V - I_sR_s)} \quad (2)$$

where I_0 and I_s are the initial current and steady-state current, R_0 and R_s are the interfacial resistance before and after polarization, respectively, and ΔV is the potential difference (10 mV).

The battery performance of the separators was examined by using LFP|separator|Li cells, which was assembled in a glove box. The testing voltage was 2.5 to 3.9 V.

Results and discussion

The hollow SnO_2 nanospheres were synthesized through a solvothermal method. XRD was utilized to characterize the crystal structure and phase purity of the as-synthesized hollow SnO_2 nanospheres. As demonstrated in Fig. 1a, its (110), (101), (211) and other diffraction peaks are consistent with the standard XRD patterns of SnO_2 (PFD: 00-41-1445) with a tetragonal rutile structure. Moreover, the absence of additional peaks indicates that the hollow SnO_2 nanospheres exhibit high phase purity. The hollow SnO_2 nanospheres were further characterized by X-ray photoelectron spectroscopy (XPS). As shown in Fig. 1b, two distinct peaks at 495.36 eV and 486.96 eV are observed, corresponding to SnO_2 $3d_{3/2}$ and SnO_2 $3d_{5/2}$, respectively. These peaks confirm the formation of Sn^{4+}, thereby validating the successful formation of SnO_2. Additionally, the absence of the Cl 2p peak in the XPS spectrum confirms the complete removal of the Cl element (Fig. S1†). The as-prepared white SnO_2 powder consists of uniform nanospheres, as displayed in Fig. 1c. Moreover, a size analysis of 100 hollow SnO_2 nanospheres reveals a normal distribution pattern, with an average diameter of 478 nm (Fig. S2†). The morphology of hollow SnO_2 nanospheres was further examined by TEM. As shown in Fig. 1d, it is indicated that the SnO_2 features a uniform spherical shape, which is consistent with the results from SEM images. Moreover, it could be seen that the edge of nanospheres is darker than the center, suggesting the hollow structure of the SnO_2 nanospheres. Moreover, the shell thickness of SnO_2 is about 120 nm from the SEM image of the broken SnO_2 (Fig. S3†). The distinct lattice fringes observed in the HRTEM image (Fig. 1e) reveal that the lattice spacing of adjacent lattice planes is 0.335 nm, corresponding to the (110) plane of the tetragonal rutile structure of SnO_2. Fig. 1f shows the nitrogen adsorption–desorption isotherm of hollow SnO_2 nanospheres. The hollow SnO_2 nanospheres demonstrate a type-IV adsorption/desorption isotherm at $P/P_0 > 0.4$, accompanied by type H2(b) hysteresis loops within the P/P_0 range of 0.45 to 0.98. Furthermore, the specific surface area of SnO_2 is measured to be 32.56 $m^2\ g^{-1}$. The pore size distribution presented in Fig. S4† exhibits that the hollow SnO_2 nanospheres possess a porous structure with an average pore size of 6.0 nm, attributed to the interstitial spaces between constituent nanoparticles during the assembly of the nanospheres. The SnO_2 with a porous structure can absorb more electrolytes, and the increased specific surface area amplifies the availability of active sites, thereby optimizing the interaction with Li.

The EAA separator was prepared based on the previously developed procedure. The slurry with EAA and PEG 2000 in THF was bladed on the glass substrate at 60 °C. After drying for 1 min at 60 °C and then template etching, the original EAA separator was prepared. The EAA@SnO_2 separator was fabricated *via* a spraying method using slurry comprising hollow SnO_2 nanospheres and PAA in a mass ratio of 10 : 1 (Fig. 2a). The concentration of the hollow SnO_2 nanospheres in the slurry was 2.5 mg mL^{-1}. As shown in Fig. 2b, the hollow SnO_2 nanospheres are distributed uniformly on the

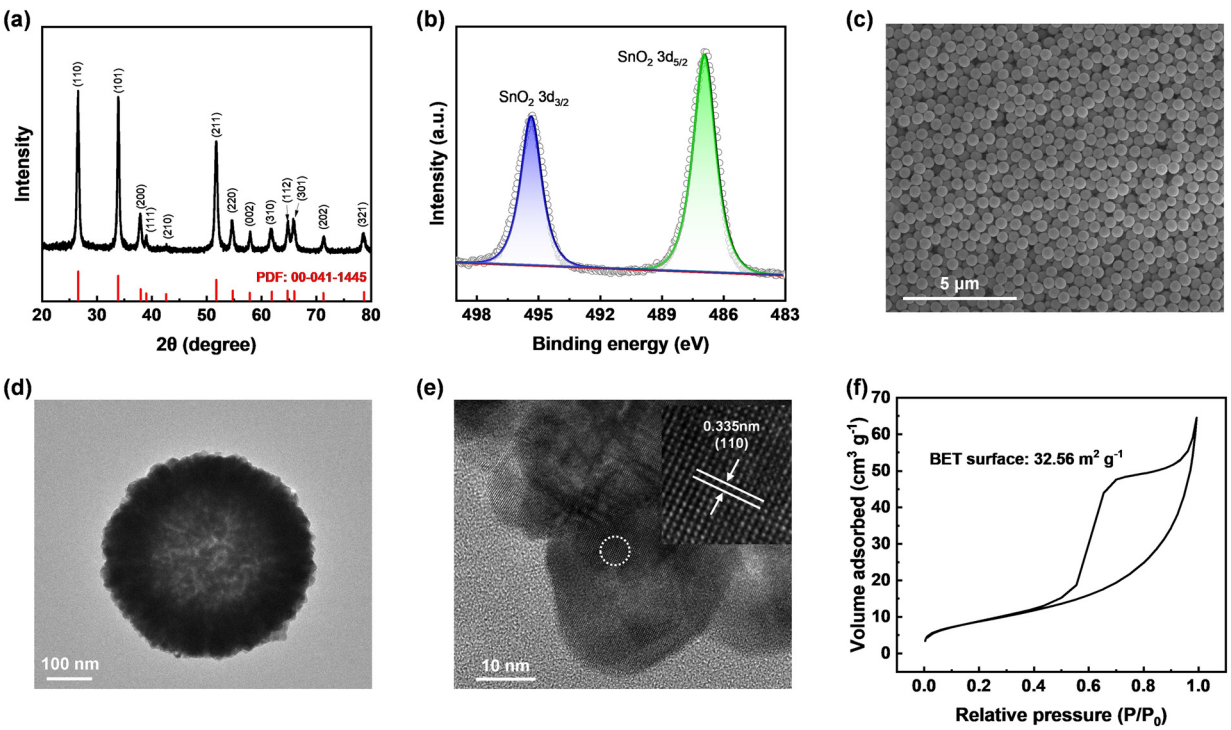

Fig. 1 Characterization of hollow SnO_2 nanospheres. (a) XRD pattern (standard card: PFD: 00-41-1445); (b) XPS spectrum of Sn 3d; (c) SEM image; (d) TEM image; (e) HRTEM image; (f) nitrogen adsorption–desorption isotherm.

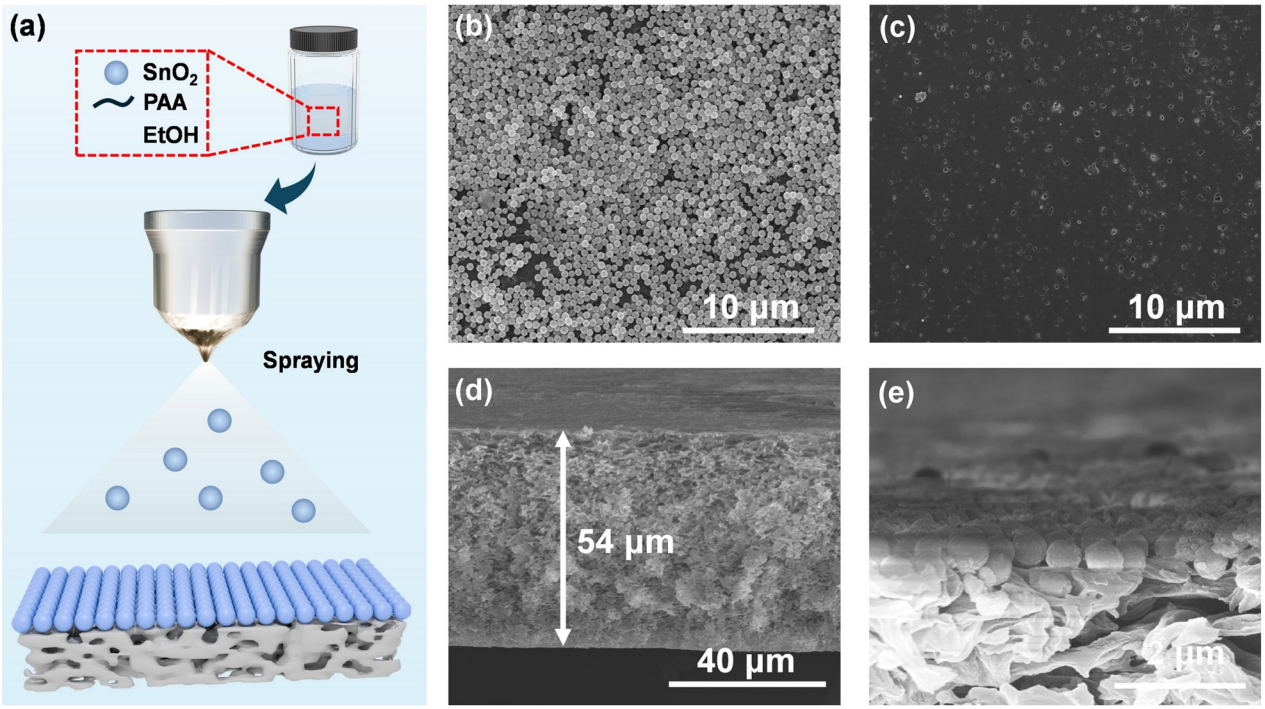

Fig. 2 (a) Fabrication process of EAA@SnO_2 separators. SEM images of the (b) coating side and (c) uncoated EAA side of EAA@SnO_2 separators. (d) Cross-section and (e) the enlarged cross-section SEM images of EAA@SnO_2 separators.

surface of EAA. Moreover, the uncoated side shows the porous morphology of the EAA matrix (Fig. 2c). The cross-section SEM image illustrates that the thickness of the EAA@SnO_2 separator is 54 μm, with the SnO_2 layer being so thin that it is nearly invisible (Fig. 2d). Moreover, the enlarged cross-sectional SEM image shown in Fig. 2e demonstrates that the SnO_2 fits tightly on the EAA separator with about 1 layer of hollow SnO_2 nanospheres on the surface. Correspondingly, this suggests that the thickness of the distinct SnO_2 coating layer is about 400–600 nm with a weight of 1.41 mg cm^{-2}.

The introduction of inorganic nanoparticles enhances the physical properties of the EAA@SnO_2 separators. As illustrated in Fig. 3a and S5,† the contact angle of the EAA@SnO_2 separator is 34°, which is lower than those of PE (45°) and EAA (41°). The carboxyl groups on EAA enhance the polarity of the polyolefin backbone, thereby improving its wettability with electrolytes. Additionally, the superior wettability of hollow SnO_2 nanospheres further reduces the contact angle of the separator with the electrolyte, enabling a better interaction between the electrode and electrolyte. Consequently, the electrolyte uptake of the separator exhibits a trend analogous to that of the contact angle. Due to the high porosity of the EAA separator, its electrolyte uptake is 111.2%, higher than that of PE (92.2%). Furthermore, the incorporation of hollow SnO_2 nanospheres, with their hollow structure and interstitial gaps, enhances electrolyte uptake, resulting in an electrolyte uptake of 122.6% for the EAA@SnO_2 separator. The thermal stability of EAA@SnO_2 was evaluated by thermogravimetric analysis (TGA). As displayed in Fig. S6,† EAA@SnO_2 remains thermally stable up to 400 °C, with 5.20% of the residual mass attributed to SnO_2. Li||stainless steel (SS) cells, equipped with different separators, were assembled to evaluate the electrochemical stability of separators through LSV analysis. As shown in Fig. 3b, all the separators are electrochemically stable at a voltage of U = 2.5–4.0 V, which is consistent with the operational voltage window of LMBs. Moreover, as displayed in Fig. 3c, the SS||SS cells were further assembled to estimate the ionic conductivity of separators through EIS measurements. Due to the increased thickness of EAA and EAA@SnO_2 separators, their bulk resistances are higher than that of PE. However, the ionic conductivity of the EAA@SnO_2 separator reaches 0.56 mS cm^{-1}, which is the highest among these separators. This enhanced performance can be attributed to the improved electrolyte uptake and the lithiophilicity of SnO_2. Similarly, the t_{Li^+} of the EAA@SnO_2 separator increases as well. As illustrated in Fig. 3d and e and S7,† the t_{Li^+} of the EAA@SnO_2 separator reaches 0.74, which is higher than that of the EAA separator. In addition to the anchoring effect of carboxyl groups on EAA towards PF_6^-, hollow SnO_2 nanospheres play a crucial role in facilitating the transport of Li^+. The narrow pores in hollow SnO_2 nanospheres selectively allow Li^+ to pass through while permitting the diffusion of PF_6^- and solvents. Moreover, the Li_xSn alloys formed through electrochemical reactions exhibit superior lithiophilicity, facilitating the rapid transport of Li^+. Consequently, based on Sand's time, the improved t_{Li^+} of the EAA@SnO_2 separators is expected to exhibit the most effective dendrite inhibition compared with EAA and PE

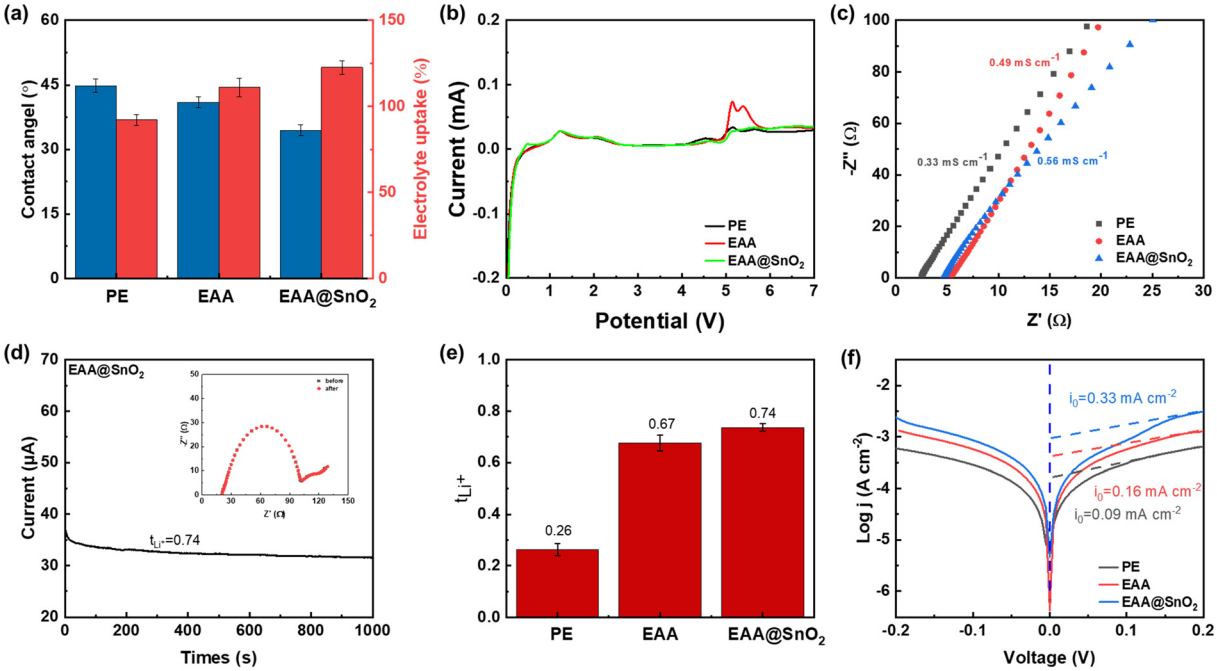

Fig. 3 (a) The contact angles of various separators with electrolytes. (b) The LSV curves of PE, EAA and EAA@SnO_2 separators, respectively. (c) The EIS spectra of PE, EAA and EAA@SnO_2 separators, respectively. (d) Chronoamperometry profile of the EAA@SnO_2 separator. The inset is the EIS spectra before and after polarization. (e) The t_{Li^+} of PE, EAA and EAA@SnO_2 separators, respectively. (f) The Tafel plots from Li||Li cells with PE, EAA and EAA@SnO_2 separators, respectively.

separators. The charge-transfer kinetics are further enhanced by the presence of SnO_2. As displayed in Fig. 3f, the exchange current density (j_0) of the EAA@SnO_2 separator is 0.33 mA cm^{-2}, twice that of EAA separators. It is attributed to the high lithiophilicity of SnO_2, which promotes the Li^+ deposition.

Li||Li symmetric cells were assembled with PE, EAA and EAA@SnO_2 separators to investigate the Li plating/stripping behaviours. The cells were filled with a carbonate-based electrolyte (1 M $LiPF_6$ in EC : DEC = 1 : 1 vol/vol) and tested at a current density of 0.5 mA cm^{-2} and 1 mA h cm^{-2}. As shown in Fig.4a, the cell with the PE separator exhibits stable cycling for over 300 h, after which an increase in voltage is observed, ultimately leading to failure after 400 h. The Li|EAA|Li and Li|EAA@SnO_2|Li cells demonstrate a stable cycling for over 1000 hours, attributed to their enhanced t_{Li^+}, which effectively suppresses dendrite growth. Notably, the voltage hysteresis of the EAA@SnO_2-based cell is as low as 17 mV, whereas that of EAA-based cells is 25 mV. This improvement can be attributed to the lithiophilicity of SnO_2, which facilitates the formation of Li_xSn alloys ($0 \leq x \leq 4.4$) upon Li^+ intercalation. The Li_xSn alloys exhibit enhanced electron conductivity, thereby mitigating the voltage hysteresis observed in the EAA@SnO_2-based cells. The morphology of Li anodes in Li|EAA@SnO_2|Li cells after 100 h cycling at 0.5 mA cm^{-2} was analysed to investigate the impact of hollow SnO_2 nanospheres on the electrode morphology. As shown in Fig. 4b, the electrode in contact with the EAA side of the EAA@SnO_2 separator demonstrates a uniform Li deposition, although some minor holes are observed. In contrast, the electrode facing the SnO_2 side displays a smooth, defect-free SEI (Fig. 4c). It is because that SnO_2 undergoes a reaction with Li^+ to initiate the formation of Sn, which subsequently reacts to generate Li_xSn alloys through the above two-step process. These alloys facilitate the Li^+ flux and promote the formation of a uniform SEI. Moreover, as illustrated in Fig. 4d, the hollow SnO_2 nanospheres maintain their structures after cycling, indicating that the hollow structure of SnO_2 effectively prevents the volume expansion, showing no negative effect on the regulation of the Li^+ flux. Besides, $LiPF_6$ is uniformly distributed across the EAA@SnO_2 separator especially in the regions containing hollow SnO_2 nanospheres from the EDX mapping (Fig. S8†). *In situ* Li symmetric cells were further studied to observe the Li deposition behaviour. As shown in Fig. S9,† the PE separator-assembled cell exhibits loose Li deposition with significant and uncontrollable dendrite formation within 600 s at a high current of 3 mA. In contrast, the Li deposition of cells using EAA separators is denser, though some dendrites are still present. Notably, the Li|EAA@SnO_2|Li cell shows a dense and uniform lithium deposition with minimal dendrite formation, indicating enhanced suppression of lithium dendrites (Fig. 4e). The inherent lithiophilicity of SnO_2 promotes the formation of Li_xSn alloys and enhances electron transport within the SEI, contributing to a more uniform and stable SEI layer.

The LFP||Li cells with various separators were assembled to evaluate the electrochemical performance of the EAA@SnO_2 separators. Cyclic voltammetry (CV) was utilized

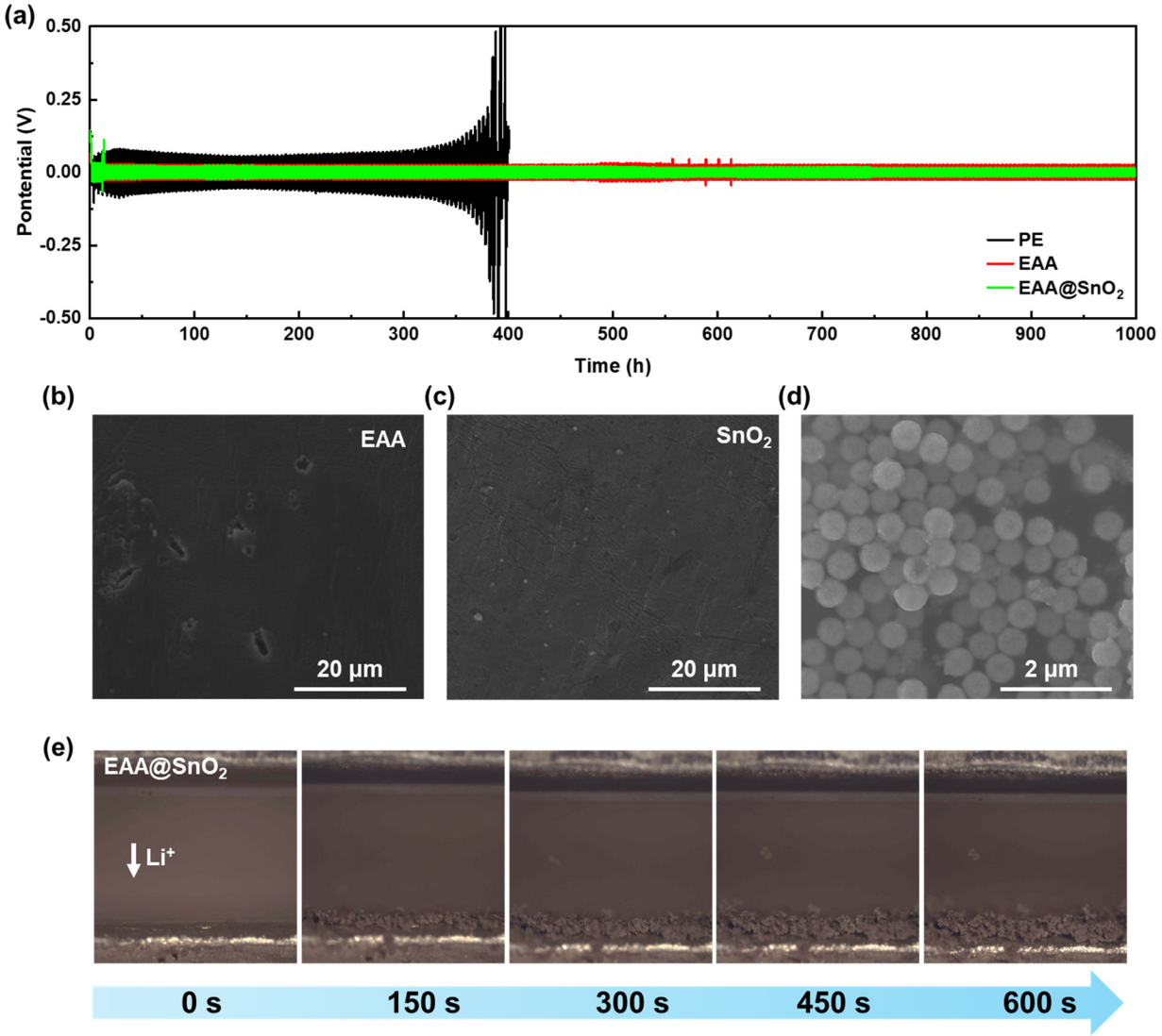

Fig. 4 (a) Voltage–time curves of Li|PE|Li, Li|EAA|Li and Li|EAA@SnO_2|Li symmetric cells at current densities of 0.5 mA cm^{-2} and 1 mA h cm^{-2}. The SEM images of the Li anode facing the (b) EAA side and (c) SnO_2 side after cycling for 100 h. (d) The SEM image of the EAA@SnO_2 separator facing the SnO_2 side after cycling. (e) The morphology evolution of the *in situ* Li||Li symmetric cells with the EAA@SnO_2 separator at a current of 3 mA.

to reflect the redox ability of the EAA@SnO_2-based cell. As shown in Fig. S10,† the redox peaks of 3.55 V and 3.33 V refer to the reaction of the LFP electrode, illustrating the cycling reactivity of the cells. Moreover, the intensity of redox peaks is increased with cycling, representing the activation process of hollow SnO_2 nanospheres transforming into Li_xSn alloys. As displayed in Fig. 5a, the initial capacity of the LFP|EAA@SnO_2|Li cell reaches 151.0 mA h g^{-1} at 1C, significantly exceeding the capacities of the EAA (142.4 mA h g^{-1}) and PE (141.3 mA h g^{-1}) separator-assembled cells. In particular, the LFP|EAA@SnO_2|Li cell demonstrates an outstanding capacity retention of 54.83% after 1000 cycles at 1C, which is higher than that of the EAA separator (45.44%) and nearly 2 times higher than that of the PE separator (30.36%). The rate performances were also tested for these separator-assembled LFP||Li cells. As shown in Fig. 5b and c, the rate capacities of the LFP|EAA@SnO_2|Li cell are 153.4, 144.2, 129.3, 118.2, 110.3 and 103.2 mA h g^{-1} at 0.5, 1, 2, 3, 4 and 5C, respectively. Moreover, the LFP|EAA@SnO_2|Li cell shows a characteristic charge–discharge profile, with cell polarization progressively increasing as the current density is elevated. Here, the impact of the SnO_2 layer thickness was further evaluated by preparing EAA@SnO_2 separators with an increased thickness of 2 μm (EAA@SnO_2-TH). As shown in Fig. S11,† the cell with the EAA@SnO_2-TH separator exhibits an inferior rate capacity compared to the EAA@SnO_2 separator, indicating that the increased SnO_2 thickness elongates the ion transport path and thereby compromise the battery performance. Notably, the EAA@SnO_2-based LFP||Li cell demonstrates a significantly higher capacity at 5C compared to EAA and PE-based cells, underscoring its superior high-rate performance. This is attributed to the ability of SnO_2 to enhance electron transport on the anode, while the generated Li_xSn alloys effectively adjust the electric field distribution and reduce the interfacial

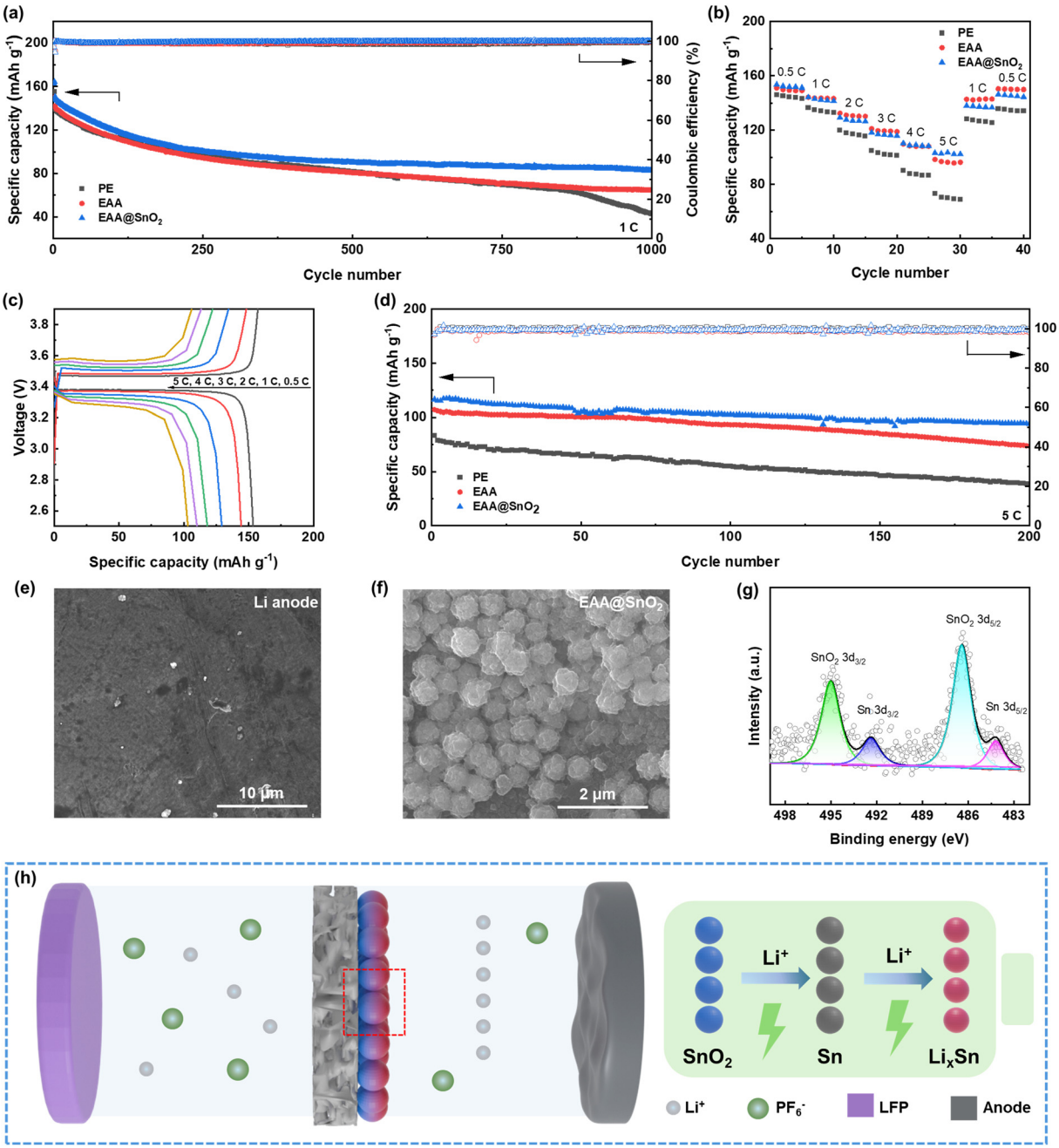

Fig. 5 (a) The long-term cycling performance of PE, EAA and EAA@SnO_2 assembled LFP||Li cells at 1C. (b) The rate capacity of LFP|PE|Li, LFP|EAA|Li and LFP|EAA@SnO_2|Li cells from 0.5C to 5C. (c) The charge–discharge profiles of LFP|EAA@SnO_2|Li cells from 0.5C to 5C. (d) The long-term cycling performance of PE, EAA and EAA@SnO_2 assembled LFP||Li cells at 5C. The SEM images of the (e) Li anode and (f) EAA@SnO_2 separator after cycling for 100 cycles at 1C in LFP|EAA@SnO_2|Li cells. (g) The XPS spectrum of Sn 3d for EAA@SnO_2 separators after cycling for 100 cycles at 1C in LFP|EAA@SnO_2|Li cells. (h) The mechanism scheme of EAA@SnO_2 separators.

impedance.[39] Thus, the long-term cycling performance at a high rate of 5C was evaluated. As illustrated in Fig. 5d, the capacity of the EAA@SnO_2-based cell is 116.6 mA h g^{-1}, significantly better than those of EAA and PE-based cells. Notably, the capacity retention of EAA@SnO_2 reaches 80.96% after 200 cycles, almost double that of the PE separator (46.46%), highlighting the superior high-rate performance of EAA@SnO_2. Similarly, the conductive Li_xSn alloys formed on the separator enhances Li^+ transport, facilitating the rapid and uniform Li^+ deposition, which effectively supports high-rate performance. Cells with a high LFP loading of 11.25 mg cm^{-2} were tested to evaluate the performance of the EAA@SnO_2 separators. As shown in Fig. S12,† the EAA@SnO_2-based cell operates steadily for over 60 cycles at 1C with a steady coulombic efficiency. In contrast, the cells using EAA and PE separators exhibit rapid capacity decay

after 25 and 40 cycles, accompanied by fluctuations in Coulombic efficiency, highlighting the excellent dendrite inhibiting capability of the EAA@SnO_2 separator.

To assess dendrite suppression of the separator and confirm the structural stability of hollow SnO_2 nanospheres on the EAA@SnO_2 separator, SEM analysis was employed to investigate the surface morphologies of the anode and separator after 100 cycles at 1C. As shown in Fig. 5e, a uniform Li deposition is observed on the anode, illustrating the homogenous Li^+ flux from the Li_xSn alloys. In addition, a dense and thin Li deposition is observed from the LFP|EAA@SnO_2|Li cell in the cross-section SEM images of the Li anode (Fig. S13a†). However, a dense but thick Li deposition is observed from the LFP|EAA|Li cell while the LFP|PE|Li cell exhibits a loose Li deposition (Fig. S13b and c†), further emphasizing the superior dendrite suppression of the EAA@SnO_2 separator. Notably, the hollow SnO_2 nanospheres retain their morphology from the SEM image of the cycled EAA@SnO_2 separator (Fig. 5f), indicating that the hollow structure provides sufficient space to accommodate volume expansion. Moreover, as displayed in the EDX mapping in Fig. S14,† the distribution of F and P from the electrolyte coincides with that of SnO_2 on the cycled separator, suggesting that the hollow SnO_2 nanospheres retain a significant amount of electrolyte, which contributes to their hollow structure and enhances the battery performance. XPS was conducted to confirm the reactions involved in the transformation of SnO_2 into Li_xSn alloys. As shown in Fig. 5g, peaks of Sn in Sn 3d XPS are observed in addition to SnO_2, indicating the reaction between SnO_2 and Li. Besides, the presence of Li_2O peaks in the Li 1s XPS spectrum further supports this transformation (Fig. S15†). The XRD pattern of the cycled EAA@SnO_2 separator also exhibits two distinct diffraction peaks at approximately 30° and 32° (Fig. S16†), which can be indexed to Li_xSn alloys ($Li_{22}Sn_5$ PDF: 00-018-0753), confirming the generation of Li_xSn alloys during cycling. In addition, XPS was also performed on the Li anode to investigate the effect of SnO_2 on SEI formation. As shown in Fig. S17,† the absence of Sn signals in XPS indicates that SnO_2 does not participate in the formation of the SEI. This also illustrates the excellent structural stability of SnO_2 during cycling. Furthermore, thanks to the high lithiophilicity of Li_xSn alloys, the charge transfer impedance (R_{ct}) of the EAA@SnO_2-based cell decreases significantly to 38 Ω from 79 Ω after 100 cycles at 1C, whereas the R_{ct} of EAA and PE increases after cycling (Fig. S18†).

Therefore, the EAA matrix and SnO_2 coating work synergistically to enhance the ability of separators to suppress the dendrite formation. As shown in Fig. 5h, the incorporation of hollow SnO_2 nanospheres, subsequently converted to Li_xSn alloys through a two-step reaction which are listed in eqn (3) and (4), leads to the formation of lithiophilic Li_xSn alloys. Li_xSn alloys enhance ionic rectification and generate a uniform electric field between the anode and separator, which facilitates a homogeneous Li^+ flux. Meanwhile, the EAA increases the t_{Li^+} with carboxyl groups and promotes the desolvation of $LiPF_6$, which leads to an increase in free Li^+ and enhances their transport. Moreover, the structural modification of hollow SnO_2 nanospheres significantly promotes Li^+ transport as well and effectively regulates Li^+ flux, ultimately resulting in a stable, dendrite-free anode and markedly improved high-rate performance.

$$SnO_2 + 4Li^+ + 4e^- \rightarrow Sn + 2Li_2O \quad (3)$$

$$xLi^+ + xe^- + Sn \rightarrow Li_xSn(0 \le x \le 4.4) \quad (4)$$

Conclusions

In summary, lithiophilic hollow SnO_2 nanospheres are coated on the EAA separator, improving the electrolyte uptake and wettability. Benefiting from the synergistic effects of carboxyl groups in the EAA matrix and the SnO_2 coating layer, the EAA@SnO_2 separator achieves a t_{Li^+} of 0.74. The hollow SnO_2 nanospheres regulate the Li^+ flux, benefiting the formation of a flat SEI. Furthermore, during cell operation, the SnO_2 transforms into Li_xSn alloys through a two-step reaction. The lithiophilic nature of the generated Li_xSn alloys enhances Li^+ transport and improves the high-rate performance of assembled cells. As a result, the EAA@SnO_2-based cells deliver a stable Li plating/tripping of over 1000 h with a low voltage hysteresis of 17 mV at 0.5 mA cm^{-2}. The LFP|EAA@SnO_2|Li cell achieves a high discharge capacity of 116.6 mA h g^{-1} at 5C, with a capacity retention of 80.96% after 200 cycles. These findings present a novel metallic coating material for separators, which enables high performance and dendrite-free LMBs.

Data availability

The data that support the findings of this study are available from the corresponding author upon reasonable request.

Author contributions

Y. C. and H. N. conceived the idea and designed the EAA@SnO_2 separators. Y. C. and H. N. have designed the experiments. Y. C., X. Z., Y. Y. and X. W. have conducted the experiments. Y. C. has drafted the article, and all authors contributed to the final manuscript.

Conflicts of interest

There are no conflicts to declare.

Acknowledgements

The authors acknowledge financial support from the Major International (Regional) Joint Cooperation Research Project of the National Natural Science Foundation of China (52020105012), the Young Scientists Fund of National Natural Science Foundation of China (52303084), and the Young

Scientists Fund of Natural Science Foundation of Hubei Province (2023AFB220) and analytical and testing assistance from the Analysis and Testing Center of HUST.

Notes and references

1 J. Feng, J. Wang, Q. Gu, P. Li, H. Xu, Y. Deng and P. Gao, *Adv. Funct. Mater.*, 2025, **35**, 2412287.
2 Y. Mu, Y. Chu, Y. Shi, C. Huang, L. Yang, Q. Zhang, C. Li, Y. Feng, Y. Zhou, M. Han, T. Zhao and L. Zeng, *Adv. Energy Mater.*, 2024, **14**, 2400725.
3 Q. Zhang, B. Hou, X. Wu, X. Li, Z. Guo, J. Liu, D. Cao, X. Huang, J. Duan, D. Mo, J. Liu and H. Yao, *Adv. Energy Mater.*, 2024, **14**, 2401377.
4 S. Zheng, S. Bi, Y. Fu, Y. Wu, M. Liu, Q. Xu and G. Zeng, *Adv. Mater.*, 2024, **36**, 2313076.
5 X. Wu, S. Zhang, X. Xu, F. Wen, H. Wang, H. Chen, X. Fan and N. Huang, *Angew. Chem.*, 2024, **136**, e202319355.
6 W. Tang, T. Zhao, K. Wang, T. Yu, R. Lv, L. Li, F. Wu and R. Chen, *Adv. Funct. Mater.*, 2024, **34**, 2314045.
7 W. Xin, J. Xiao, J. Li, L. Zhang, H. Peng, Z. Yan and Z. Zhu, *Energy Storage Mater.*, 2023, **56**, 76–86.
8 L. Cao, M. Chu, Y. Li, X. Xu, Y. Qiu, Y. Dai, C. Sun, Z.-X. Huang, X.-L. Wu and H. Geng, *Adv. Mater.*, 2024, **36**, 2406034.
9 J. Lee, S. H. Jeong, J. S. Nam, M. Sagong, J. Ahn, H. Lim and I.-D. Kim, *EcoMat*, 2023, **5**, e12416.
10 B. Ma, H. Zhang, R. Li, S. Zhang, L. Chen, T. Zhou, J. Wang, R. Zhang, S. Ding, X. Xiao, T. Deng, L. Chen and X. Fan, *Nat. Chem.*, 2024, **16**, 1427–1435.
11 Y. Li, Q. Qu, L. Lv, J. Shao and H. Zheng, *Adv. Funct. Mater.*, 2024, **34**, 2314100.
12 T. Wang, B. Chen, C. Liu, T. Li and X. Liu, *Angew. Chem., Int. Ed.*, 2024, **63**, e202400960.
13 M. Yao, Q. Ruan, S. Pan, H. Zhang and S. Zhang, *Adv. Energy Mater.*, 2023, **13**, 2203640.
14 A. Du, H. Lu, S. Liu, S. Chen, Z. Chen, W. Li, J. Song, Q.-H. Yang and C. Yang, *Adv. Energy Mater.*, 2024, **14**, 2400808.
15 D. Kang, S. Sardar, R. Zhang, H. Noam, J. Chen, L. Ma, W. Liang, C. Shi and J. P. Lemmon, *Energy Storage Mater.*, 2020, **27**, 69–77.
16 H. Song, J. Lee, M. Sagong, J. Jeon, Y. Han, J. Kim, H.-G. Jung, J.-S. Yu, J. Lee and I.-D. Kim, *Adv. Mater.*, 2024, **36**, 2407381.
17 H. Jia, C. Zeng, H.-S. Lim, A. Simmons, Y. Zhang, M. H. Weber, M. H. Engelhard, P. Gao, C. Niu, Z. Xu, J.-G. Zhang and W. Xu, *Adv. Mater.*, 2024, **36**, 2311312.
18 Y. Ji, L. Dong, J. Liu, H. Xie, S. Zhong, C. Yang, J. Han and W. He, *Energy Environ. Sci.*, 2024, **17**, 4078–4089.
19 Y. Ji, C. Yang, J. Han and W. He, *Adv. Energy Mater.*, 2024, **14**, 2402329.
20 X. Lin, R. Baranwal, G. Ren and Z. Fan, *Chem. Eng. J.*, 2024, **500**, 157192.
21 K. Wang, T. Zhao, R. Lv, W. Tang, T. Yu, G. Chen, L. Li, F. Wu and R. Chen, *Adv. Energy Mater.*, 2024, **14**, 2401281.
22 L. Zuo, Q. Ma, P. Xiao, Q. Guo, W. Xie, D. Lu, X. Yun, C. Zheng and Y. Chen, *Adv. Mater.*, 2024, **36**, 2311529.
23 A. Jung, M. J. Lee, S. W. Lee, J. Cho, J. G. Son and B. Yeom, *Small*, 2022, **18**, 2205355.
24 X. Wang, Y. Wen, Y. Wang, Y. Chen, L. Yang, C. Guo, H. Nie, X. Zhou and X. Xie, *J. Power Sources*, 2024, **615**, 235126.
25 Y. Liu, X. Tao, Y. Wang, C. Jiang, C. Ma, O. Sheng, G. Lu and X. W. Lou, *Science*, 2022, **375**, 739–745.
26 Z. Zhang, J. Wang, H. Qin, B. Zhang, H. Lin, W. Zheng, D. Wang, X. Ji and X. Ou, *ACS Nano*, 2024, **18**, 2250–2260.
27 D. Li, Y. Ouyang, Y. Xiao, Y. Xie, Q. Zeng, S. Yu, C. Zheng, Q. Zhang and S. Huang, *Adv. Funct. Mater.*, 2024, **34**, 2314296.
28 L. Zhou, H. Pan, G. Yin, Y. Xiang, P. Tan, X. Li, Y. Jiang, M. Xu and X. Zhang, *Adv. Funct. Mater.*, 2024, **34**, 2314246.
29 S. A. Han, H. Qutaish, J.-W. Lee, M.-S. Park and J. H. Kim, *EcoMat*, 2023, **5**, e12283.
30 G. Yu, Y. Cui, S. Lin, R. Liu, S. Liu, Y. Zhu and D. Wu, *Adv. Funct. Mater.*, 2024, **34**, 2314935.
31 S. Yao, Y. Yang, Z. Liang, J. Chen, J. Ding, F. Li, J. Liu, L. Xi, M. Zhu and J. Liu, *Adv. Funct. Mater.*, 2023, **33**, 2212466.
32 M. Du, Z. He, Y. Zhang, Y. Cai and Q. Zheng, *Adv. Energy Mater.*, 2025, 2403674.
33 X. Li, K. Liu, N. Dong, B. Liu, G. Tian, S. Qi and D. Wu, *Chem. Eng. J.*, 2024, **481**, 148525.
34 X. Zeng, Y. Chen, H. Nie, Y. Yang, J. Chen, H. Pei, X. Wang, Y. Yang, J. Pang, X. Zhou, G. Wang and X. Xie, *Small*, 2025, **21**, 2411626.
35 D. Li, D. Shi, K. Feng, X. Li and H. Zhang, *J. Membr. Sci.*, 2017, **530**, 125–131.
36 Q. Zhao, R. Zhou, C. Wang, J. Kang, Q. Zhang, J. Liu, Y. Jin, H. Wang, Z. Zheng and L. Guo, *Adv. Funct. Mater.*, 2022, **32**, 2112711.
37 Y. Chen, P. Mickel, H. Pei, Y. Wen, X. Guan, Y. Wang, X. Wang, O. A. Mhtachem, C. Zhang, H. Nie, X. Zhou, P. Kral and X. Xie, *ACS Appl. Mater. Interfaces*, 2023, **15**, 18333–18342.
38 Y. Liu, S. Xiong, J. Wang, X. Jiao, S. Li, C. Zhang, Z. Song and J. Song, *Energy Storage Mater.*, 2019, **19**, 24–30.
39 Y. Ma, F. Wu, N. Chen, Y. Ma, C. Yang, Y. Shang, H. Liu, L. Li and R. Chen, *Chem. Sci.*, 2022, **13**, 9277–9284.
40 H. Lee, X. Ren, C. Niu, L. Yu, M. H. Engelhard, I. Cho, M.-H. Ryou, H. S. Jin, H.-T. Kim, J. Liu, W. Xu and J.-G. Zhang, *Adv. Funct. Mater.*, 2017, **27**, 1704391.
41 C. Yue, S. Sun, M. Jang, E. Park, B. Son, H. Son, Z. Liu, D. Wang, U. Paik and T. Song, *Electrochim. Acta*, 2021, **370**, 137703.
42 H. G. Nam, J. Y. Park, J. M. Yuk and S. M. Han, *Energy Storage Mater.*, 2022, **45**, 101–109.
43 Y. Xiang, Z. Wang, W. Qiu, Z. Guo, D. Liu, D. Qu, Z. Xie, H. Tang and J. Li, *J. Membr. Sci.*, 2018, **563**, 380–387.
44 N. Hu, X. Lv, Y. Dai, L. Fan, D. Xiong and X. Li, *ACS Appl. Mater. Interfaces*, 2018, **10**, 18665–18674.
45 X.-D. Zhu, C. Han, J. Zhang, W. Mi, Y. Qin, J. Gao, J. Wu, J.-J. Zou, X. Yang, Y.-C. Zhang and G. Wu, *EcoMat*, 2023, **5**, e12291.
46 J. Kim, S. Lee, J. Kim, J. Park, H. Lee, J. Kwon, S. Sun, J. Choi, U. Paik and T. Song, *Carbon Energy*, 2024, **6**, e610.
47 D. Ding, H. Tao, X. Fan, X. Yang and L. Fan, *Adv. Funct. Mater.*, 2024, **34**, 2401457.
48 F. Liang, H. Dong, Z. Ji, W. Zhang, H. Zhang, C. Cao, H. Li, H. Liu, K.-Q. Zhang, Y. Lai, Y. Tang and M. Ge, *Sci. China Mater.*, 2023, **66**, 1736–1746.